Landfast ice controls on turbulence in Antarctic coastal seas

JGR Oceans

Key Points:

- With landfast ice cover turbulence in the upper ocean is reduced by a factor of four, and near-inertial and tidal energy by factor two
- Turbulent heat and nutrient fluxes are seasonal, and 6 (heat) and 10 (nutrients) times greater than previous estimates
- The Antarctic under-ice boundary layer is on average as turbulent during seasonal landfast ice cover as when exposed to the wind

Correspondence to:

M. E. Inall,
mark.inall@sams.ac.uk

Landfast Ice Controls on Turbulence in Antarctic Coastal Seas

Mark E. Inall[1,2] , **J. Alexander Brearley**[3] , **Sian F. Henley**[2] , **Alexander D. Fraser**[4] , and **Sarah Reed**[1]

[1]Scottish Association for Marine Science, Oban, UK, [2]School of GeoSciences, University of Edinburgh, Edinburgh, Scotland, [3]British Antarctic Survey, Cambridge, UK, [4]Australian Antarctic Program Partnership, Institute for Marine and Antarctic Studies, University of Tasmania, Hobart, TAS, Australia

Abstract Knowledge of the ocean surface layer beneath Antarctic landfast ice is sparse. In this article surface layer turbulent and fine structure are quantified with and without landfast ice at the same West Antarctic Peninsula location. Landfast ice reduced turbulence levels locally to an order of magnitude less than ice-free values, and near-inertial energy and sub-inertial tidal energy levels to less than half their ice-free values. Vertical turbulent heat and nutrient fluxes were, respectively, 6 and 10 times greater than previously estimated. Under-ice tidal energy dissipation over the entire Antarctic continental shelf due to seasonal landfast ice cover is estimated to be between 788 MW to ~6 GW. The total rate of wind-generated turbulence in the surface ocean is greatly reduced by the presence of seasonal landfast ice to an average of 14% of the ice-free value, but with large sectoral variations. Counter-intuitively, however, tides and wind contribute approximately equally to the turbulent kinetic energy budget of the upper ocean between the Antarctic coastline and the maximal landfast ice extent, with large sectoral variations, attributed to geographic variations in the strength of the barotropic tide.

Plain Language Summary Coastal oceans are generally well-mixed near their surface due to wind, and near the seabed due to tidal currents. A rigid, fixed surface of sea ice that is attached to the land (landfast ice) renders the ocean surface a more quiescent environment. However, we show that turbulence drives significant upward winter transfer of heat and nutrients. We also show counter-intuitively that around the coastal zones of the Antarctic, landfast ice results in an ocean surface layer made as turbulent by the unceasing rhythm of the tides as by the sporadic action of the wind.

1. Introduction

The Ocean Surface Boundary Layer (OSBL) is subject to momentum, turbulent kinetic energy (TKE) and buoyancy fluxes from the atmosphere, lending it strong seasonality (Belcher et al., 2012; Evans et al., 2018; Lucas et al., 2019). This is nowhere more apparent than in high latitudes where the ocean surface may freeze seasonally to form a rigid upper boundary, especially where that ice is pinned to land. The under-ice OSBL has been much studied in terms of its turbulent properties and as a mediator of air/sea momentum transfer (Fer & Sundfjord, 2007; Martin et al., 2014; McPhee, 1999, 2008). However, to the best of the authors' knowledge, no previous studies have investigated the turbulent properties of the OSBL at the same location under contrasting conditions of 100% landfast ice cover and completely ice-free (open ocean) conditions: we do so here, evaluating vertical heat and nutrient fluxes at the base of the OSBL, and then estimate and discuss implications for the $\sim 4 \times 10^5$ km^2 of Antarctic coastal seas subject to seasonal landfast ice cover. This is done using new observations from a location on the West Antarctic Peninsula (WAP) taken during summer and winter, and using pan-Antarctic landfast ice cover maps, a high-resolution Southern Ocean State Estimate (SOSE) and global hourly wind reanalyzes to drive a simple one-dimensional ocean mixing model. A schematic of the processes under consideration is shown in Figure 1, including a depiction of the seasonal migration of landfast ice cover and representative profiles of temperature and dissolved inorganic nutrients from the WAP.

1.1. WAP Ice Cover

In common with all Antarctic coastal regions, the WAP shelf seas (Figure 2) exhibit strong seasonal ice cover, superimposed on both interannual variability and effects of global warming. Much of the warming is known to be ocean-driven, with consequential melting of ice shelves and marine-terminating glaciers (Cook et al., 2016). The extent and duration of WAP summer sea ice has decreased rapidly since the start of the satellite era (Henley
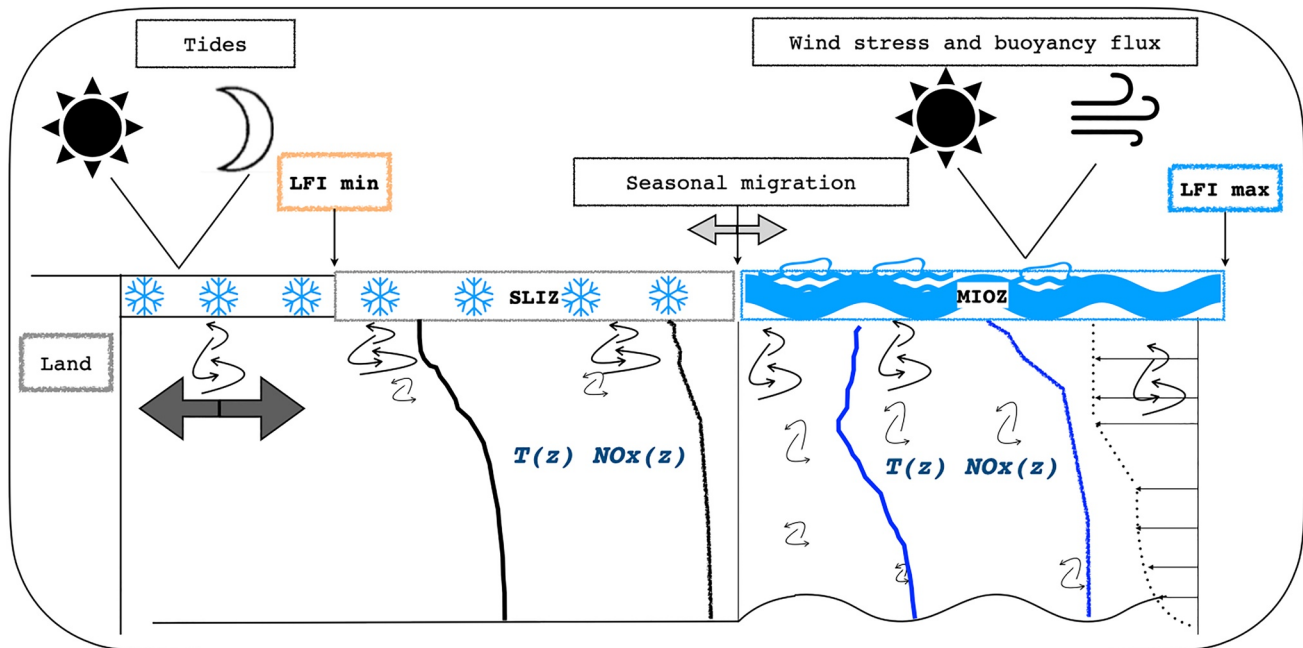
Figure 1. Schematic of the key physical drivers of the ocean surface boundary layer under seasonally varying landfast ice cover, depicting the full landfast ice zone from minimum to maximum extents, the seasonal landfast ice zone (SLIZ), and the mobile ice/open ocean zone (MIOZ). Typical winter (under SLIZ, in black) and summer (under MIOZ, in blue) profiles of temperature and dissolved inorganic nutrients are also shown, redrawn to scale in Figure 3. Dark gray arrows represent tides, light gray the seasonal movement of the landfast ice edge and curved arrows turbulence.

et al., 2019). Any impacts this may have on landfast ice cover remain largely unquantified, though landfast ice cover in the East Antarctic and Indian Ocean sectors is reported to have increased between 2000 and 2018 (Fraser et al., 2020). Unlike East Antarctica (Fraser et al., 2012), variability of landfast ice in other Antarctic sectors was poorly described until the recent availability of a circum-Antarctic dataset of landfast ice cover, a valuable
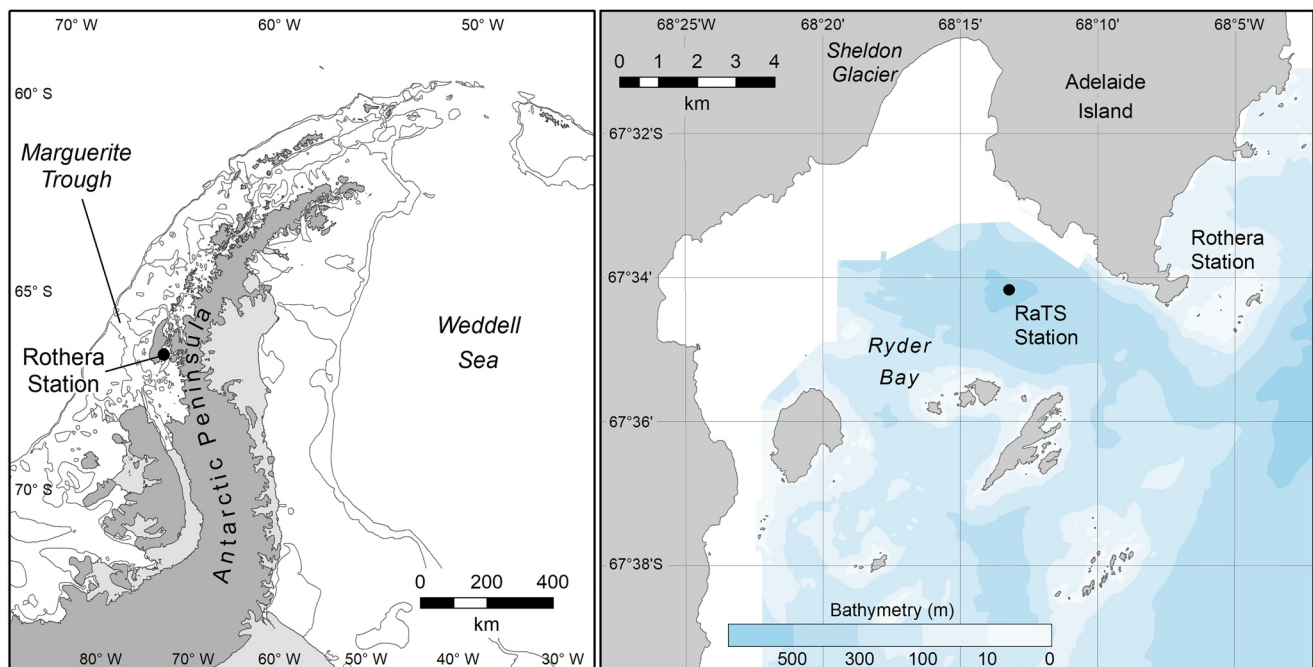
Figure 2. Maps of West Antarctic Peninsula and of Ryder Bay. Locations of the Rothera time series site (RaTS Station) and Rothera research station are indicated.

resource used in this article (Fraser et al., 2020). Positive trends in landfast ice extent have since been reported in the Dronning Maud Land, Western Indian Ocean, Australian and Bellingshausen Seas sectors (newly defined regions); all positive trends are significant (Fraser et al., 2021). Visual observations from Rothera Station (Figure 2) indicate that smooth, thermodynamically formed landfast ice covers Ryder Bay completely during most winter seasons with significant variability in the duration and extent of cover (Venables & Meredith, 2014).

1.2. WAP Upper Ocean

The WAP OSBL heat budget is determined in part by the turbulent flux of heat from upper circumpolar deep water (uCDW). Sourced in the Antarctic Circumpolar Current of the Southern Ocean, uCDW intrudes onto the continental shelf through a complicated system of canyons (Moffat et al., 2009), and is the primary nutrient source to WAP ecosystems (Henley et al., 2017; Prézelin et al., 2000; Serebrennikova & Fanning, 2004). uCDW temperature, salinity and nutrients exhibit weak seasonality beneath strongly seasonal Antarctic surface waters (AASW) (Moffat & Meredith, 2018; Venables et al., 2013). Ryder Bay (Figure 2) is a 520 m deep embayment separated from Marguerite Trough by a number of topographic ridges, which restrict deeper exchanges (Venables et al., 2017) but do not constrain uCDW, which is readily exchanged with the WAP. AASW on the other hand is locally modified, and is considered to be representative of nearshore Antarctic coastal regions which experience localized wind and glacial effects.

On the WAP, a seasonal thermocline is accompanied by a seasonal halocline formed through summer sea ice melt and glacial runoff. In autumn near-surface temperatures drop and by August sensible and latent heat losses drive the formation of a convectively-deepened winter mixed layer to 70–100 m, ultimately causing landfast ice formation in Ryder Bay as the OSBL drops to below freezing point. Freezing extracts heat from above the summertime temperature minimum (∼100 m, Figure 3). Convective mixing rarely releases heat directly from uCDW (Venables et al., 2013).

1.3. Turbulent Properties of the OSBL

Momentum and TKE enter the OSBL from wind stress, ice movement and buoyancy loss. Melt layers stratify the near-surface and may alter the near-inertial energy distribution, and modify ice/ocean drag via internal wave generation and ice flow form drag, for example, Martin et al. (2014). OSBL measurements reported here span periods of zero ice cover and 100% landfast ice cover; we therefore focus on the contrast between the presence and the absence of a fixed rigid lid of landfast ice, excluding explicit representation of mobile pack ice in marginal ice zones, although the effects are estimated in the analyses and discussion.

The motivation behind this work was to answer the following questions: (a) What are the quantitative differences between turbulence dissipation rates during landfast ice-covered and open water periods? (b) How does a rigid landfast ice lid change the dissipation rate budget, its vertical profile and consequent scalar fluxes of heat and nutrients? (c) What do the controlling processes tell us about the turbulent state of the pan-Antarctic landfast ice OSBL?

Direct observations were made to address questions (a) and (b). Landfast ice maps, global atmospheric reanalyzes, an ocean state estimate, a tidal model and a simple ocean mixing model are combined to address question (c).

2. Instruments and Data

Observations at the same location as the Ryder Bay Rothera time series (RaTS, 67.570°S 68.225°W, Figure 2) comprise: (a) Repeated profiles to 300 m of shear microstructure (Prandke & Stipps, 1998) from a small boat in February 2016 and through an artificial ice-hole in August 2016; (b) a moored upward-looking, 75 kHz RDI Instruments acoustic doppler current profiler (ADCP); (c) dissolved inorganic nutrients from discrete water samples in February 2016, and for ice-covered conditions from 2013, 2014 and 2015 (Henley et al., 2020). For circum-Antarctic analyses resources are: ERA5 hourly winds (Hersbach et al., 2020); bi-weekly landfast ice maps (Fraser et al., 2020); the CATS2008 inverse tidal model (Padman et al., 2008); a new version of the SOSE (Mazloff et al., 2010); and the PWP one dimensional ocean mixing model (Alford, 2020; Price et al., 1986).
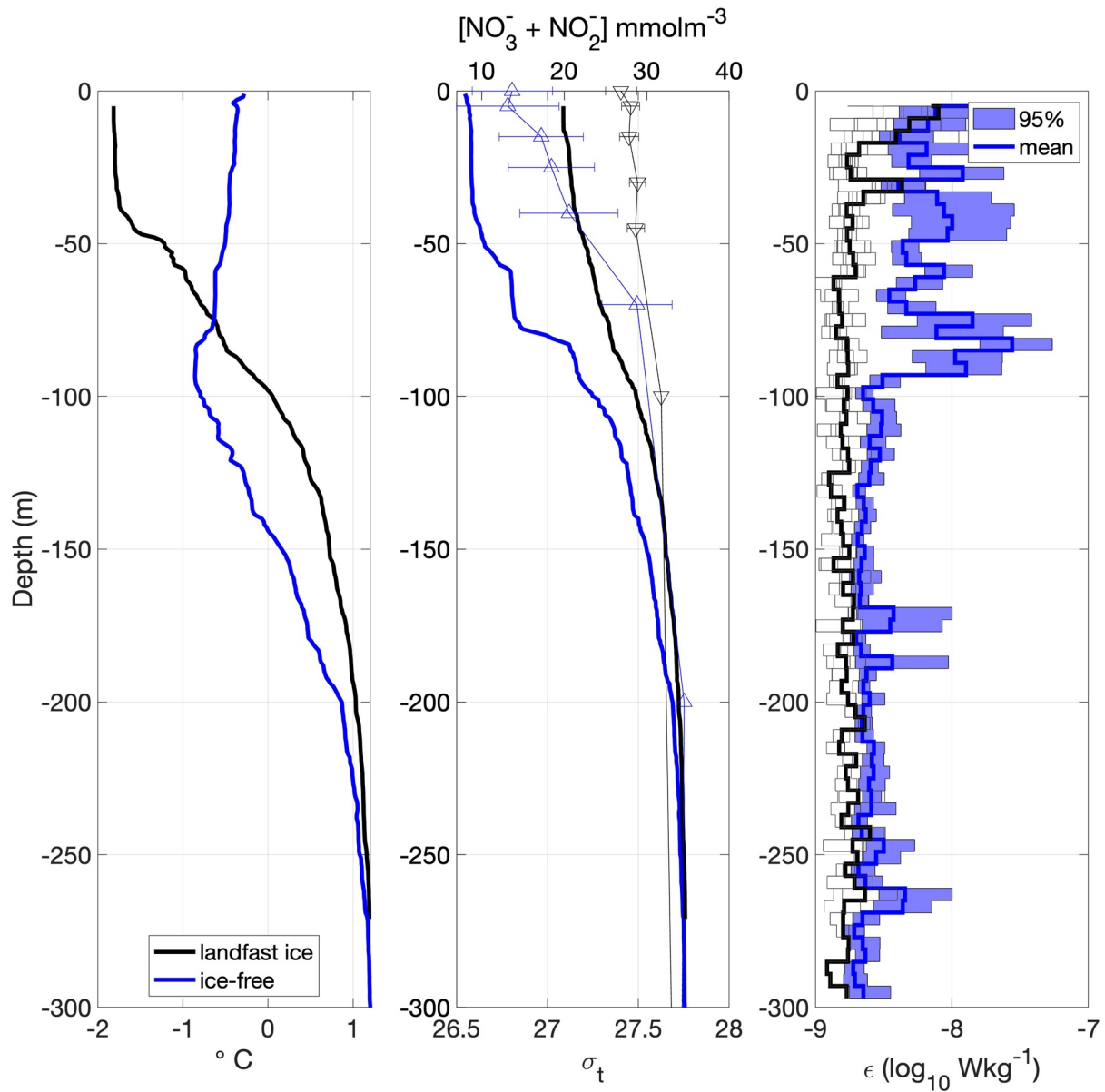
Figure 3. Winter (black) and summer (blue) profiles of: temperature (left); σ_t and NO_x mean and one standard deviation (middle); turbulent kinetic energy dissipation rate mean and 95% confidence intervals (right).

3. Methodologies and Their Application

3.1. Dissipation Measurements and Vertical Turbulent Flux Estimation

Free-falling shear microstructure profilers are commonly used to quantify turbulence levels in the water column. Quantification of TKE dissipation, through direct microstructure measurement or through scaling of fine scale measurements, permits the calculation of vertical fluxes of heat, salt, nutrients and momentum. In summer 2016, a small (5.5 m) open boat was used to collect 47 MSS90 microstructure profiles at the RaTS site in Ryder Bay over a 17-day period (6–23 February 2016). A total of nine MSS90 profiles in winter were made at the RaTS site through a 1×1 m hole cut through the landfast sea ice. All winter profiles were taken on a single day (17 August 2016) and over a 90-min period, coinciding with maximal current flow of the locally dominant K1 tide (as derived from the ADCP record). A standard methodology was used to estimate the rate of dissipation of turbulent kinetic energy (TKE dissipation, ϵ, units W kg^{-1}). The methodology involves time series measurements at 416 Hz of velocity shear from the very near-surface (~3 m) to 300 m depth with a loosely tethered MSS90

probe (Prandke & Stipps, 1998), free-falling with a vertical speed of ∼0.8 ms^{-1}. Two microstructure shear sensors mounted at the front of the probe resolve vertical shear in the horizontal velocity from scales of approximately 0.005–0.5 m. Variance of the shear, $\left(\frac{\partial u}{\partial z}\right)^2$, is calculated by integrating the shear spectra over the inertial subrange (from 2 to 100 cpm, or to the Kolmogorov wave number, whichever is the lower of the two). Shear variance was calculated for every 2 m segments of data (approximately 2.5 s of data or 1,000 data points) with a 50% overlap between adjacent segments. Estimates of ϵ were then derived using the well-established relationship for isotropic turbulence $\epsilon = 7.5\mu \left(\frac{\partial u}{\partial z}\right)^2$, where μ is the temperature-dependent dynamic viscosity of seawater. The method returns vertical profiles of ϵ with a resolution of 1 m, with 50% overlap between adjacent values. Estimates of the vertical eddy diffusivity (K_z) for vertical heat flux calculations were made from the vertical profiles of ϵ using the relationship $K_z = \Gamma\epsilon/N^2$, with $\Gamma = R_f/(1 - R_f)$ (Osborn, 1980) and using a flux Richardson number of $R_f = 0.17$, a value commonly used in geophysical applications (Shih et al., 2005). Profiles of the buoyancy frequency squared (N^2) were calculated on ordered density profiles.

Vertical heat fluxes were estimated, in Wm^{-2}, according to $Q = \rho C_p K_z \partial T/\partial z$, averaged between 70 and 90 m in summer (across the $\sigma_t = 27.2$ surface) and between 45 and 55 m in winter ($\sigma_t = 27.05$). For comparison with previously published fine-scale heat flux estimates (Brearley et al., 2017), summer and winter averages between 100 and 200 m were also computed, representing the upward heat flux out of the uCDW. Error bounds on $\epsilon(z)$ and $K_z(z)$ were estimated using a bootstrapping procedure on the 47 profiles taken during summer see for example, Rippeth and Inall (2002). For the nine winter profiles the mean, maximum and minimum values recorded at each depth level are displayed (due to the smaller number of observations in winter). Summer and winter profiles of temperature, salinity, density, nutrients (as nitrate concentration) and ϵ are shown in Figure 3.

Discrete-depth water samples were taken in summer 2016 and in the winters of 2013, 2014, 2015 and analyzed for dissolved inorganic nutrients including nitrate and nitrite (Henley et al., 2017). No dissolved inorganic nutrient data are available for winter 2016. Values for nitrate + nitrite (hereafter NO_x, units of mmol m^{-3}) were regressed against potential density (σ_t) measured simultaneously by the CTD at the same depths as each bottle sample. Correlation was high, with $r^2 = 0.88$ (0.86), $n = 53$ (18), and regression gradient $m = 19.4$ (22.7) mmol m^{-3} (kg m^{-3})$^{-1}$ for summer (winter). With high confidence in the linearity of the density-NO_x regressions, a simplified expression is used: $NO_{x\ \text{flux}} = m\Gamma\epsilon\rho/g$ (mmol m^{-2} s^{-1}), following Sharples et al., (2007). As for heat fluxes, nutrient fluxes into the OSBL were computed as averages between 70 and 90 m in summer (across the $\sigma_t = 27.2$ surface) and between 45 and 55 m in winter ($\sigma_t = 27.05$).

Moored ADCP data were collected in 30-min ensemble intervals, with velocities recorded in 37 16 m bins. Prior to analysis, velocities were corrected using observed sound speeds at the transducer face, and the resultant velocities were transformed from magnetic to Earth coordinates by application of a +6.2° declination angle. Individual ensembles whose "percentage good" threshold fell below 50% were excluded, as was the near-surface velocity bin, which was of consistently poor quality. Velocity spikes were removed by a two-stage process. First, velocities greater than 2 m s^{-1} were excluded, then adjacent values were removed as spikes if they differed by more than a tolerance range of four. Quality controlled ADCP data were then separated into upper (23–100 m) and lower (150–300 m) layers, rotary spectral analysis was applied, revealing contrasting regimes between landfast ice covered and ice-free periods, above and below the halocline (Figure 4).

3.2. Landfast Ice Zone

Regions of the ocean which are seasonally covered and uncovered by landfast ice are referred to as the seasonal landfast ice zone (SLIZ, Figure 1). Bi-weekly landfast ice maps are available at 1 km resolution spanning the period 2000–2018 (Fraser et al., 2020). For 2016 the extent over the full Antarctic domain (LFImax, Figure 1) was 5.58×10^5 km^2 on 27 September 2016 and the minimum (LFImin) was 1.72×10^5 km^2 on 16 March 2016. Sectoral figures were also determined (Table 1). The difference between the LFImax and LFImin defines the SLIZ, which varies in area from zero (when LFImin occurs) to a maximum value equal to the difference between LFImax and LFImin. To determine bi-weekly SLIZ maps, only grid cells for which landfast ice cover was not present in every landfast ice mask for 2016 were selected. Finally, a seasonal mobile pack ice/open ocean zone (MIOZ) is defined as the region between LFImax and the (bi-weekly) SLIZ edge at a particular point in time.
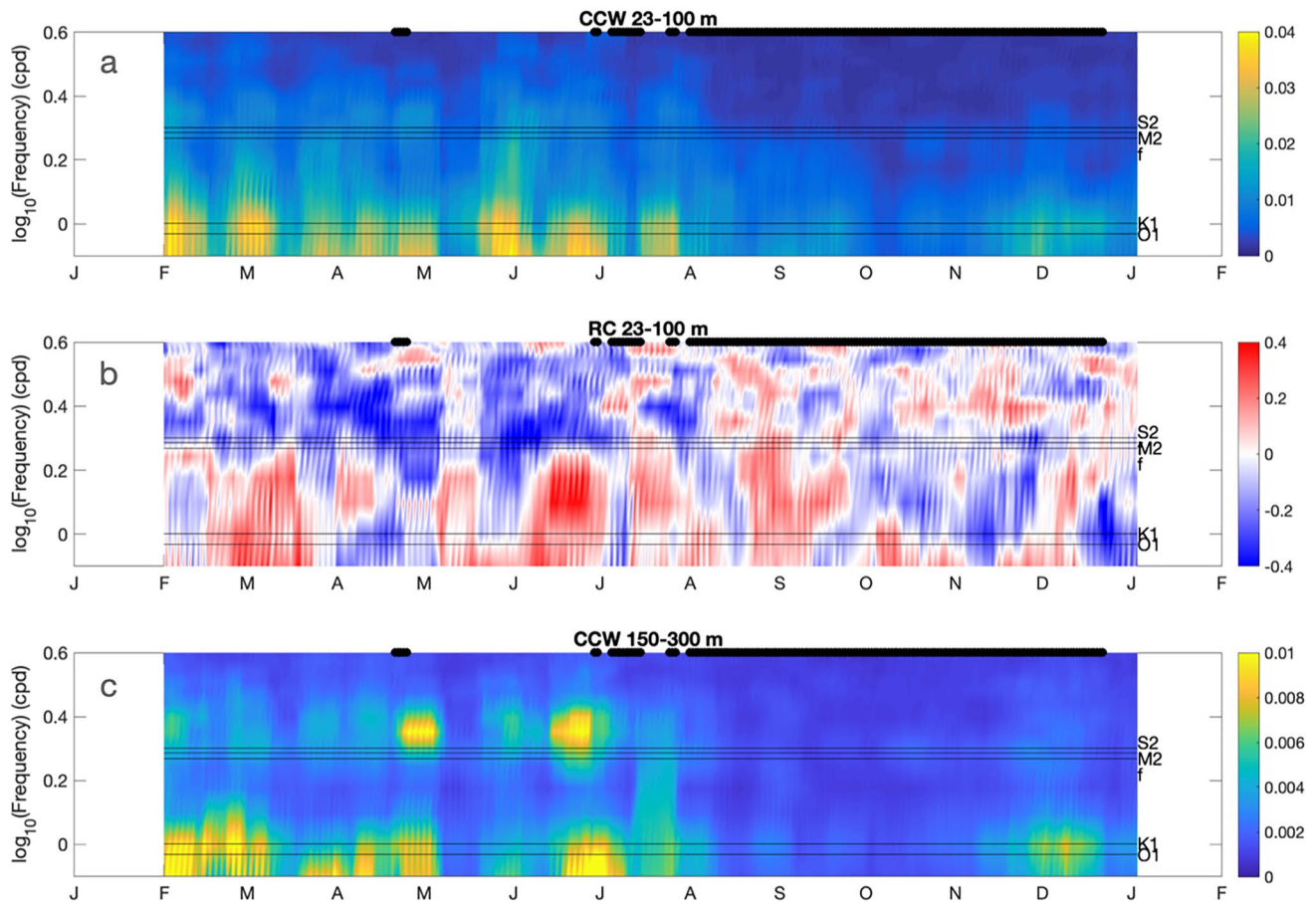
Figure 4. (a) Upper water column counter clock-wise (CCW) rotary spectra of velocities ($\log_{10}$ scale). (b) Upper water column, ratio of depth-averaged rotary coefficients ($\log_{10}$(CW/CCW)) evaluated from 30-day overlapping spectra evaluated each day. (c) Lower water column CCW rotary spectra of velocities ($\log_{10}$ scale, bottom). Fast-ice-cover indicated by black overbar.

Table 1
Circum-Antarctic and Sector Breakdown for the Year 2016

Sector	Ice min 10^5 km²	Ice max 10^5 km²	Mean water depth (m) at max ice extent	$\sum W_{MOIZ}$ MW	T_{LFI} MW	$\sum W_{SLIZ}$ MW
Full Antarctic	1.72	5.58	369 ± 258	955	788	−5,698
	16 March	27 September				
Bellingshausen and Amundsen seas (WAP). 60°W–130°W	0.50	1.12	386 ± 231	84.7 (528)	11.6 (72.4)	−637 (−3,963)
	15 February	29 July				
Ross Sea 130°W–160°E	0.23	0.80	327 ± 240	81.8 (554)	72.9 (494)	−393 (−2660)
	15 February	13 August				
Western Pacific 160°E–90°E	0.42	2.05	399 ± 267	539 (1,276)	336 (795)	−3,283 (−7,773)
	16 March	14 July				
Indian Ocean 90°E–20°E	0.26	1.46	340 ± 238	276 (886)	164 (526)	−1,774 (−5,706)
	01 March	27 September				
Weddell Sea 20°E–60°W	0.15	0.53	340 ± 312	104 (1,053)	109 (1,109)	−358 (−3,640)
	16 March	27 September				

Note. Maximum and minimum landfast ice extent, area and timing. Mean and standard deviation of water depth beneath landfast ice (at max extent). Wind and tide related dissipation totals for full antarctic domain, and by sector. Sectoral figures also presented normalised (in brackets) by seasonal landfast ice area change sector (LFImax minus FLImin)/Full(LFImax–LFImin).

Estimates of percentage (mobile) sea ice cover in the MIOZ from other sources (e.g., NSIDC) are not used in this study. In the following, bi-weekly area masks of LFImax, SLIZ and MIOZ are used.

3.3. Tidal Flow Boundary Layer Dissipation

The rate at which energy is dissipated via boundary layer drag is estimated, in units of W m^{-2}, using the expression, see for example (Simpson et al., 1996)

$$P_w = \rho_w C_D U_w^3 \tag{1}$$

where U_w is the flow speed at the outer edge of the boundary layer, ρ_w water density (set as a constant 1,025 kgm^{-3}), and an under-ice drag coefficient of $C_D = 1.5 \times 10^{-3}$. The value for C_D was derived directly from the measured (winter) profiles of $\epsilon(z)$ within the constant stress portion of the under-ice boundary layer and using the law-of-the-wall method (Dewey & Crawford, 1988). A value of $C_D = 1.5 \times 10^{-3}$ is within the ranges estimated by other under-ice boundary layer studies, including landfast ice studies (see review of (Lu et al., 2011) and references therein). Landfast ice can be formed either thermodynamically by local freezing, or dynamically by convergence of pack ice against a coastal boundary or existing ice edge. The underside of thermodynamically formed landfast ice is smoother than dynamically formed landfast ice. Distinguishing between the two remotely has been attempted in East Antarctica, where it was found that 67% of the total was "smooth" landfast ice, that is, thermodynamically formed (Giles et al., 2008), and in the Arctic (Segal et al., 2020). In Ryder Bay, landfast ice during 2016 was entirely smooth, thermodynamically formed landfast ice. Under-ice drag coefficients for dynamically formed landfast ice range from two to 10 times the value of $C_D = 1.5 \times 10^{-3}$ derived here, which therefore gives a lower limit on our subsequent under-ice tidal energy dissipation estimates The boundary layer drag formulation is used in our discussion section on tidal flow modulation by the landfast ice cover.

For 2016 we take both the bi-weekly LFImax and SLIZ maps and linearly interpolate onto hourly geographical masks. Landfast ice data are gridded on a 1 × 1 km grid, whereas the CATS tidal model resolution is 4 × 4 km (Padman et al., 2002). Under-ice frictional boundary energy loss is then estimated each hour for both the full landfast ice area (LFImax) and for the SLIZ. For all landfast ice cells the CATS2008 tidal model current speeds, U_{tide}, were computed at hourly intervals for the whole year (using 11 tidal constituents), by selecting the nearest tidal model grid to each ice mask cell (Figure 5 gives contours of $\log_{10} U_{\text{tide}}^3$). The ice masks are then used to calculate the total hourly TKE power loss (in W) as $T_0 = \rho_w A \ C_D U_{\text{tide}}^3$ (from Equation 1) where A is the grid cell area ($A = 1$ km^2). Finally, all power losses so computed are summed over the entire Antarctic domain, and time-averaged over the year and further broken down by Antarctic sector (Table 1).

Averaged over calendar year 2016 this method gives a total power loss under the bi-weekly LFI masks (i.e., under all landfast ice) around Antarctica of $T_{\text{LFI}} = 788$ MW. This value is interpreted as a lower limit of the annual average rate of work of the barotropic tide on the ice attributable to all landfast ice cover. If one third of landfast ice is dynamically formed, with an under-ice drag coefficient five times that of thermodynamically formed landfast ice (both reasonable possibilities), then this figure would rise by a factor of about 7.5 to $T_{\text{LFI}} \sim 6$ GW.

3.4. Wind Power Injected Into the OSBL

Direct injection of TKE into the OSBL from the wind depends on wind stress, the surface wave field and Langmuir turbulence. OSBL depth-integrated TKE dissipation, ϵ_I, is often expressed in terms of the wind-work, $\epsilon_I = \alpha E_0$, where $E_0 = \rho_w u_*^3$ is the wind-work (units of Wm^{-2}), and u_* is the water friction velocity. The parameter α, sometimes referred to as the "wave factor" (Craig & Banner, 1994), estimated using TKE observations in the OSBL, takes values ranging from $\alpha = 6.5$ to 45.5 (Fer & Sundfjord, 2007; Lozovatsky, 2005a; Oakey & Elliott, 1982). Values as high as $\alpha = 100$ have been used in modeling studies (Craig & Banner, 1994), based on current meter observations, as opposed to TKE observations (Wu, 1983). In order to estimate ϵ_I we equate the surface stress of the ocean on the atmosphere to be of equal magnitude to the stress experienced by the ocean from the wind, that is, $\rho_a C_A U_{10}^2 = \rho_w u_*^2$ for example, (Craig & Banner, 1994), where U_{10} is the 10 m wind speed, C_A the ocean surface drag coefficient which is wind speed dependent following a bulk formulation (Fairall et al., 2003), and u_* is the water friction velocity. The rate of energy loss from the 10 m wind is commonly expressed as $E_{10} = \rho_a C_A |U_{10}|^3$ (units of W m^{-2}), most of which is dissipated within the atmospheric boundary layer, directly analogous to the under-ice ocean boundary layer formulation above (Equation 1). The rate of wind-work on the
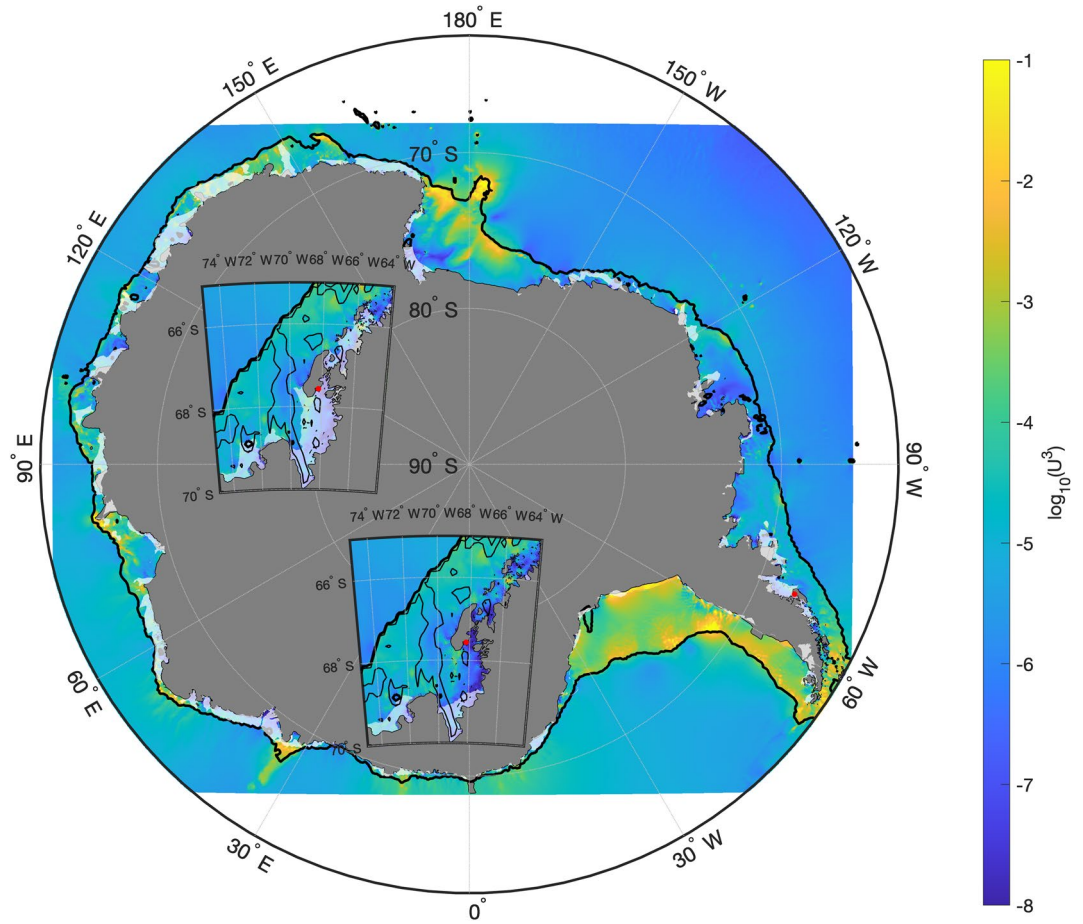
Figure 5. Full Antarctic domain with West Antarctic Peninsula (WAP) as inset, and location of Ryder Bay (red marker). Color shading is $\log_{10}(U^3)$ 2016 maximum landfast ice extent (Fraser et al., 2020) shaded white. Insets of WAP sector show minimum (15 February, lower inset) and maximum (29 July, upper inset) landfast ice extents. Thick black line is 1,000 m bathymetric contour, delineating the edge of the Antarctic continental shelf, insets also show 500 m depth contour. Whitespace around the periphery is the spatial limit of CATS2008.

OSBL, E_0, may then be evaluated from a knowledge of U_{10} and C_A as $E_0 = \rho_w u_*^3 = E_{10}\rho_w^{-1/2}(\rho_a C_A)^{1/2}$, as in (Randelhoff et al., 2017). Thus, depth-integrated TKE within the OSBL directly injected by the wind field is estimated via a knowledge of ERA5 10 m wind as,

$$\epsilon_I = \alpha E_{10}\rho_w^{-1/2}(\rho_a C_A)^{1/2}, \tag{2}$$

or

$$\epsilon_I = \alpha\rho_w^{-1/2}(C_A\rho_a)^{3/2}|U_{10}|^3, \tag{3}$$

To provide an upper bound on our estimate of ϵ_I the observationally based wave factor estimate of $\alpha = 45.5$ is used (Lozovatsky, 2005).

The rate of wind-work on the OSBL, E_O, averaged over summer and winter 2016 is shown in Figures 6 and 7, respectively. Equation 3 was evaluated at hourly intervals by interpolating ERA5 (variables U10 and V10), 10 m wind vector data, onto both the SLIZ and MIOZ masks (determined as described above), expressing the total power for each cell as $W_{\text{SLIZ/MOIZ}} = \alpha\epsilon_I$ (units of W), where the subscript denotes which mask was used. $W_{\text{SLIZ/MOIZ}}$ are then summed over all SLIZ/MIOZ grid cells to give $\Sigma W_{\text{SLIZ/MOIZ}}$. ΣW_{MOIZ} represents an estimate of mean rate of working of the wind on the ocean over the MIOZ, disregarding for the time being effects of any mobile sea ice cover, a point returned to in the discussion. On the other hand, ΣW_{SLIZ} is the hypothetical rate at
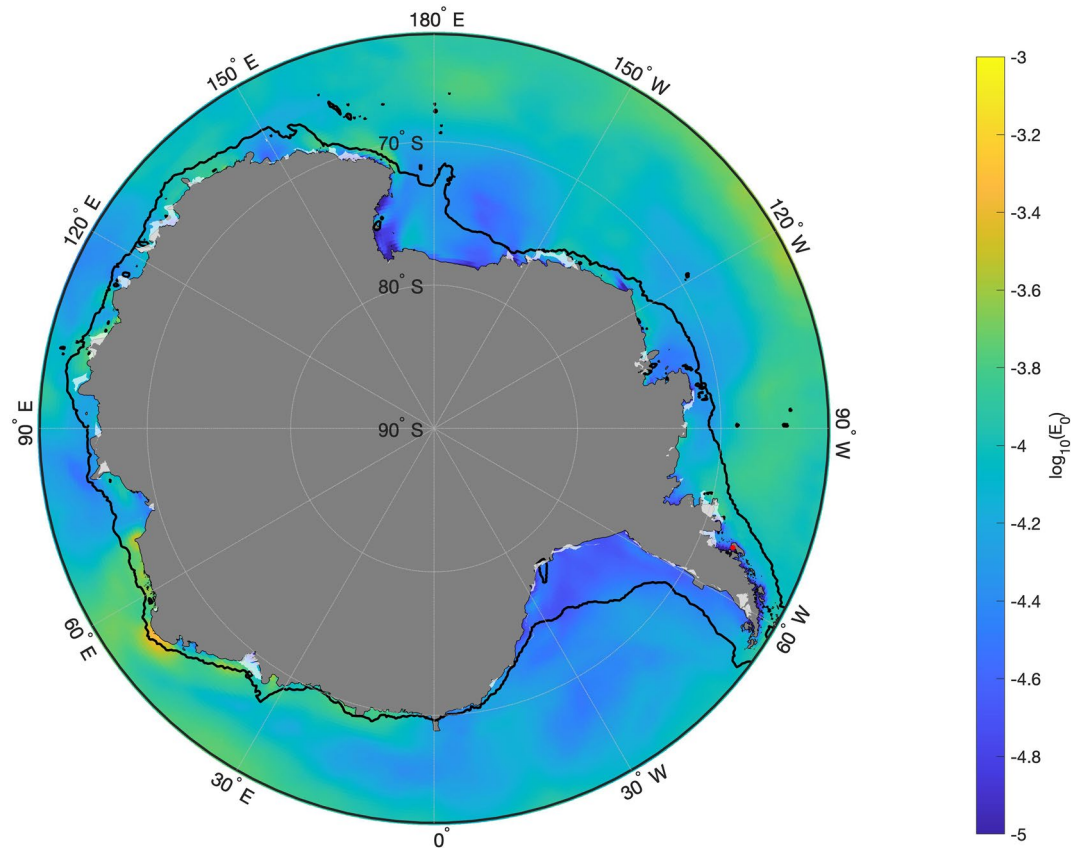
Figure 6. E_0 and minimum landfast ice averaged over the summer month of February 2016. See text for details. Same scale as used in Figure 7.

which TKE would have been injected into the SLIZ OSBL had there been no seasonal landfast ice cover, and is estimated for discussion only, since it does not represent an observed reality. Both parameters are shown as a circum-Antarctic time series (Figure 8) and a year average (Table 1) for the full Antarctic, and further broken down by Antarctic sector.

3.5. Southern Ocean State Estimate and PWP Mixing Model

The proportion of wind energy injected at the ocean surface that is available to change ocean stratification, and not dissipated as heat, is dependent on many factors in the OSBL, crucially including its thickness. Estimations of wind-driven mixing (Alford, 2020) and heat flux from beneath the OSBL are made here using the one dimensional PWP (Price et al., 1986) ocean mixing model. The model was forced with hourly ERA5 10 m winds and surface heat fluxes (Hersbach et al., 2020) and initialized with both in situ observations for comparison with Ryder Bay heat flux estimates, and with SOSE (Mazloff et al., 2010) temperature and salinity profiles for pan-Antarctic analyses.

For comparison with Ryder Bay MSS-derived heat fluxes, the PWP model was initialized with the first of the summer RaTS MSS temperature and salinity profiles (6 February 2016) and then integrated forward for 17 days (until 23 February 2016, the date of the final summer MSS cast), forced at the surface with hourly ERA5 wind stress (derived from 10 m wind using a standard formulation (Fairall et al., 2003) and with surface heat fluxes set to zero. PWP model time step was one hour and vertical grid spacing 1 m. SOSE data are not available for 2016 (Mazloff et al., 2010). However, a new higher resolution (7 km) version of SOSE for 2010 only was made available (Mazloff, pers comm), and used here with 2010 ERA5 wind data to run the PWP model for 2010. In order to isolate water column mixing due only to wind work, all surface buoyancy fluxes were set to zero (Alford, 2020), the PWP model initialized with SOSE profiles and run for consecutive 14-day periods for every MIOZ mask grid
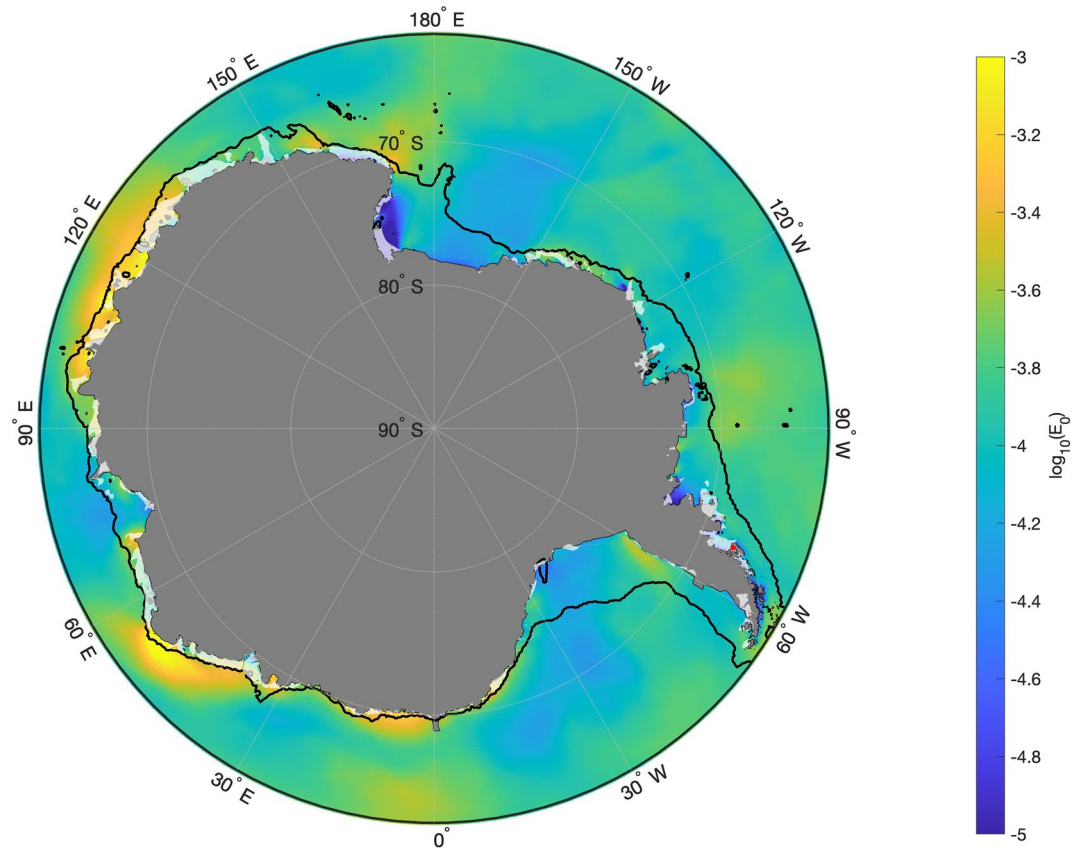
Figure 7. E_0 and maximum landfast ice averaged over the winter month of August 2016. See text for details. Same scale as used in Figure 6.

cell. For all model simulations the time rate of change of the depth integrated PE anomaly (units Wm^{-2}) and heat flux across the base of the OSBL (also units Wm^{-2}) were computed each time step and then averaged in time (all runs) and space (2010 pan-Antarctic runs). Pan-Antarctic and sectoral values are given in Table 2.

4. Analysis

In February 2016 the water column above uCDW was weakly temperature-stratified in the upper 75 m and salinity-stratified throughout (Figure 3). Stratification was maximum above the 75 m temperature minimum ($\sigma_t = 27.0$). TKE dissipation $\epsilon(z)$ was elevated in the upper layer, reducing by a factor of ~5 or 6 between 90 and 100 m, remaining at that lower level to the maximum measurement depth (300 m) (Figure 3). In mid-winter during continuous landfast ice cover, temperature was homogeneous at freezing point to 45 m and weakly salt-stratified below 15 m. Beneath 45 m, T and S increased monotonically, with a weak stratification maximum at ~100 m (the perennial halocline). In winter $\epsilon(z)$ was highest in the uppermost 15 m, and statistically indistinguishable from summer values. From 15 to 100 m $\epsilon(z)$ winter values were approximately an order of magnitude lower than the summer ice-free values. From 100 to 300 m the winter values were marginally lower than during summer (not statistically significant).

Upward heat flux out of uCDW (100–200 m, $\sigma_t = 27.54$) was $Q = +1.4$ (+0.6) Wm^{-2} in summer (winter), consistent with previous estimates of $Q \sim +1.0$ Wm^{-2} (Brearley et al., 2017; Howard et al., 2004). During summer however the heat flux into the OSBL is negative, due to the temperature minimum beneath the seasonally-warmed OSBL. Heat flux across the base of the summer OSBL (70–90 m, $\sigma_t = 27.13$) was $Q = -0.25$ Wm^{-2}, demonstrating erosion of the sub-surface summer temperature minimum both from above by seasonally warmed OSBL, and from below by uCDW. During winter the OSBL was thinner, with a strong positive temperature gradient between 40 and 50 m ($\sigma_t = 27.02$). Winter heat flux across $\sigma_t = 27.02$ was $Q = +6.4$ Wm^{-2}. Given the
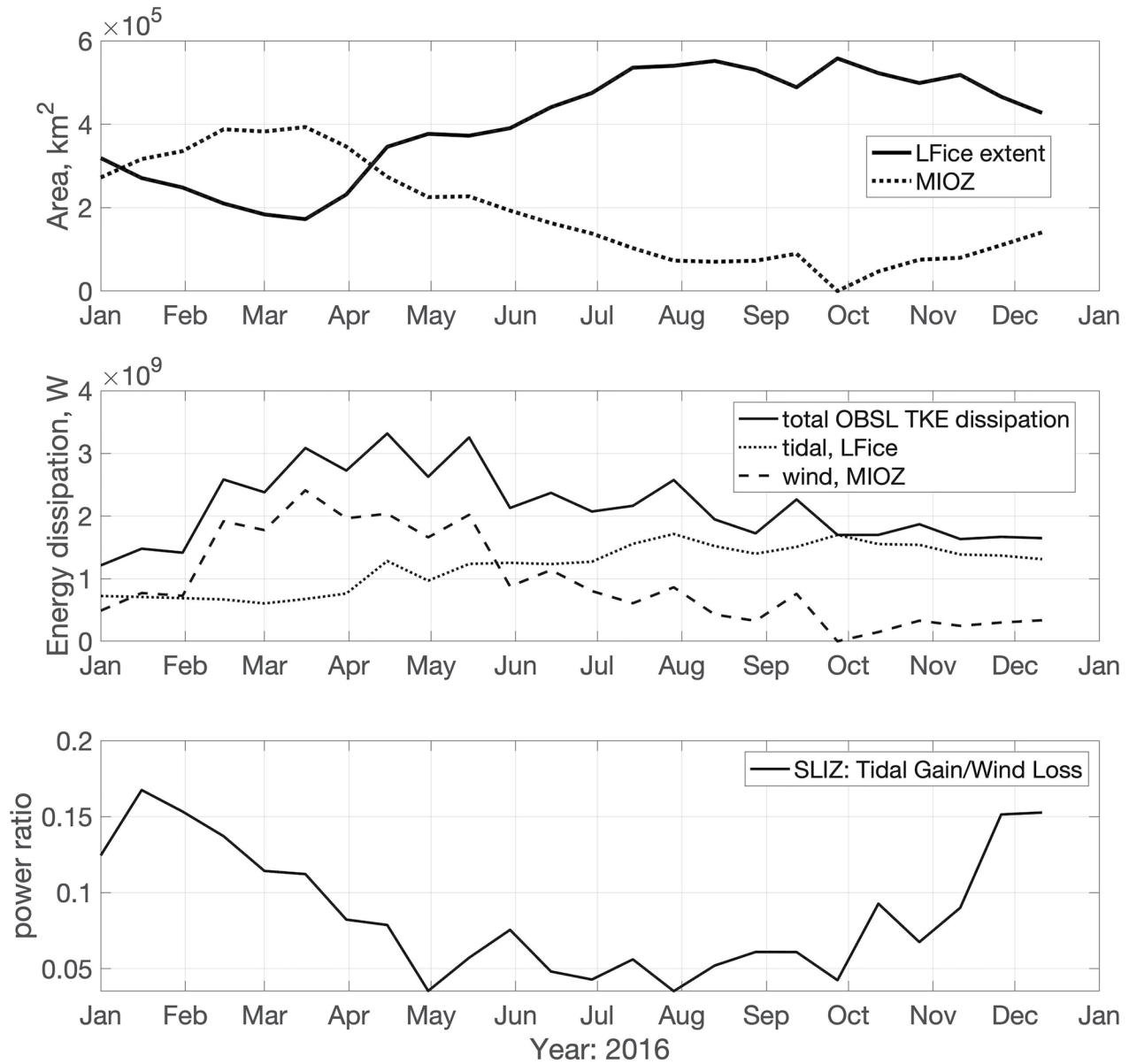
Figure 8. Upper panel: Circum-Antarctic landfast ice extent during 2016 (Fraser et al., 2020). Lower panel: Wind power insulated from direct turbulent kinetic energy injection into the ocean surface boundary layer (OSBL) by seasonal landfast ice cover, tidal power dissipated in OSBL due to seasonal landfast ice cover, and their difference. Wind power derived from ERA5 reanalysis, tidal power from CATS2008 inverse tidal model, both calculations using landfast ice maps as described in the text.

monotonic increase of temperature with depth, this figure represents the upward winter heat flux from uCDW into the landfast ice-covered OSBL.

Modeled heat flux derived from the PWP simulation from 6–23 February gave $Q_{PWP} = -0.29$ Wm^{-2}, very close to the observational estimate.

Nutrient fluxes into the OSBL are estimated as $NO_{x\ flux} = 0.34$ (0.10) mmol m^{-2} day^{-1} in summer (winter) averaged between 70 and 90 m, $\sigma_t = 27.2$ (45–55 m, $\sigma_t = 27.05$).

Analysis of the ADCP rotary spectra separated into upper (23–100 m) and lower (150–300 m) layers reveals contrasting regimes between landfast ice covered and ice-free periods, above and below the halocline (Figure 4). In the upper layer counter clock-wise (CCW) energy between diurnal (O1, K1) and semi-diurnal bands (f, M2, S2) was dramatically reduced between ice-free and landfast ice covered periods; at sub-inertial frequencies there

Table 2
Circum-Antarctic and Sector Breakdown for the Year 2010

Year 2010 PWP. sector	Ice min 10^5 km^2	Ice max 10^5 km^2	ΣW_{MOIZ} MW	Heat flux Wm^{-2}	Mixing work rate 10^{-4} Wm^{-2}	Equivalent OSBL (=100 m) dissipation 10^{-8} Wkg^{-1}
Full Antarctic	1.62	5.88	1,578	0.14	18	1.8
	02 March	28 September				
WAP. Bellingshausen and Amundsen seas. 60°W–130°W	0.117	0.682	123 (765)	0.25	33	3.3
	02 March	30 July				
Ross Sea 130°W–160°E	0.234	0.963	88 (593)	0.25	19	1.9
	02 March	13 September				
Western Pacific 160°E–90°E	0.611	2.63	950 (2249)	0.14	30	3.0
	02 March	28 September				
Indian Ocean 90°E–20°E	0.337	1.64	516 (1,661)	0.07	11	1.1
	17 March	30 Jul				
Weddell Sea 20°E–60°W	0.267	5.96	101 (1,026)	0.08	2.0	0.21
	12 December	13 September				

Note. Maximum and minimum landfast ice extent area and timing. Various annually averaged wind effects in the MIOZ derived from ERA5 wind-forced PWP mixing model: Spatially summed wind work, spatially averaged vertical heat from into the OSBL from below, mixing rate-of-work and equivalent OSBL TKE dissipation rate (see text for details). MOIZ, mobile ice/open ocean zone; OSBL, ocean surface boundary layer; WAP, West Antarctic Peninsula.

was a tendency for CW (clockwise) polarization, as previously noted (Wallace et al., 2008). In the lower layer CCW energy was an order of magnitude less than in the upper layer during the ice-free period, and essentially zero during ice-covered periods (Figure 4c).

Quantitatively, in the upper layer there were reductions in both near-inertial and sub-inertial tidal energy by more than a factor of 2 between ice-free and landfast ice covered conditions. During a brief period of ice cover in late April CCW energy in the upper layer fell markedly, further evidence of the energetic consequences of insulating the water column from wind stress.

In summary, 100% landfast ice cover: (a) coincides with a reduction of OSBL TKE below ~15 m; (b) isolates the OSBL from near-inertial energy input and; (c) reduces the energy of the dominant-period diurnal tides.

5. Discussion

5.1. Vertical Fluxes

Winter heat flux from uCDW into the under ice OSBL, $Q = +6.4$ Wm^{-2}, is a factor of 6 higher than previous estimates (Brearley et al., 2017), raising the annualized landfast ice melt estimate to ~0.7 m, a significant figure compared to formation estimates of 1.9–2.9 m per year (Venables & Meredith, 2014). This estimate derives from nine MSS profiles, made during an unexceptional period in the moored ADCP record (17th August, see Figure 4). Dissipation rates measured below the turbulent under-ice boundary layer, though low (Figure 3), were well above the noise floor of the instrument (1×10^{-9} Wkg^{-1}), and the shear spectra passed the quality control comparison to the theoretical Nasmyth dissipation spectral form (Gargett, 1985). Given uncertainties in R_f and individual ϵ measurements (generally considered to be approximately 50% of their estimated value), and that nine independent estimates were made, the heat flux error is estimated to be ~ 1 Wm^{-2}, that is $Q = +6.4 \pm 1$ Wm^{-2}. This must be seen as an instrument and method-based error estimate made over a short time period. However, the ADCP record revealed this time period to be one dominated by tidal variability, with no evidence of exceptional dynamic activity from other sources, such as remote wind influence.

In contrast, the summer OSBL is cooled ($Q = -0.25$ Wm^{-2}) by vertical mixing due to presence of the sub-surface temperature minimum, a highly typical feature of summer Antarctic shelf waters. Derived from 47 profiles, the error estimate on this value is much smaller than in winter (~ 0.1 Wm^{-2}), and given the sign of the temperature gradient, the flux can only be negative. Forced only by wind stress (with surface heat fluxes set to zero), the PWP

model estimate of heat flux into the OSBL during the same period of $Q_{\mathrm{PWP}} = -0.29\ \mathrm{Wm}^{-2}$ is remarkably close to and indistinguishable from the observed value, strongly suggesting that the observed heat flux was wind-driven rather than by other turbulent processes at the base of the OSBL (for example internal wave breaking).

Summer nitrate flux (0.34 mmol m^{-2} day^{-1}) is an order of magnitude larger than previously reported for Ryder Bay (0.04 mmol m^{-2} day^{-1}), more comparable to central WAP shelf values (0.16 – 0.56 mmol m^{-2} day^{-1}) though spatial variability is high (Henley et al., 2018). A winter nitrate flux, not previously measured, of 0.10 mmol m^{-2} day^{-1} is a factor 2 larger than the previously-reported summer values (Henley et al., 2018), though smaller than the summertime flux quantified here, due to both weaker nitrate gradients and lower winter $\epsilon(z)$ levels at the depth of the nitracline. Comparison of these new nitrate fluxes with estimates of biological nitrate uptake (~10 mmol m^{-2} day^{-1}) concur with the observed seasonal cycle of nitrate concentration (Clarke et al., 2008; Henley et al., 2017; Weston et al., 2013). Summer fluxes, much larger than previously reported, are still an order of magnitude smaller than nitrate uptake by *phytoplankton*, leading to rapid drawdown (utilization) of the nitrate pool during the *phytoplankton* growing season. Nitrate is not normally drawn down to concentrations that are limiting to *phytoplankton* growth, in part because blooms in this region are limited instead by light, iron availability and/or zooplankton grazing (Henley et al., 2020). There is also evidence for nutrient resupply to surface waters during the growing season driven by synoptic-scale mixing events (storms), advective effects and/or organic matter remineralization in nutrient resupply to surface waters (Henley et al., 2017, 2018). This is consistent with our finding that even during the un-exceptional wind conditions of February 2016 vertical turbulent fluxes into the mixed layer were wind driven. During winter, nutrient uptake is minimal due to light limitation of *phytoplankton* growth, therefore winter nitrate fluxes reported here, approximately one third of summer values, are sufficient to restore and then maintain high winter nitrate levels under landfast ice.

5.2. Contrasting Landfast Ice Cover

The analyses of Section 4 demonstrated that during ice-free periods the dynamics of the OSBL are controlled by wind stress, most energetic at periods between near-inertial and marginally super-inertial. In contrast, during landfast ice cover, the OSBL is largely controlled by law-of-the-wall turbulent boundary layer scaling, with dominant variability at tidal periods. TKE enters the OSBL via wind in the absence of ice, and via boundary stress when landfast ice is present. In Ryder Bay the OSBL was considerably less energetic in winter during landfast ice cover (Figures 3 and 4, Table 1), and it is reasonable to assume this is true for the whole Antarctic—A testable assumption.

In 2016 the seasonal change in landfast ice cover for the Antarctic was ~4×10^5 km^2 (Figure 5, Table 1), close to the climatological average cycle (Fraser et al., 2021). From the preceding boundary layer arguments, and with knowledge of wind stress and tidal currents, and using the pan-Antarctic PWP model simulations we have quantified: (a) The total tidal energy dissipated by the presence of a rigid ice lid; (b) the corresponding effective reduction in wind TKE entering the ocean due to landfast ice; (c) the comparative seasonal cycle of tide and wind sourced TKE in the SLIZ OSBL; and (d) the wind-induced heat flux into the OSBL of the SLIZ during a different calendar year (2010).

5.3. Tidal Power Input

K1 and O1 tidal currents during landfast ice cover in Ryder Bay are known to be reduced compared to their ice-free values (Brearley et al., 2017; Wallace et al., 2008); similar reductions are found in Arctic settings (Georgas, 2012; St-Laurent et al., 2008). Shelf waters exist in a quasi-equilibrium between energy input from astronomical forcing and energy loss via dissipative processes, which drive the system towards equilibrium within a few forcing periods. The majority of the world's tidal energy dissipates at solid boundaries (Egbert & Ray, 2000), and scales with the cube of current speed (U) at the outer edge of an approximately logarithmic boundary layer. Assuming similar drag coefficients for under-ice and sea-bed (an assumption later relaxed), it follows that $2U_{ic}^3 = U_{if}^3$ where *ic* denotes ice covered and *if* ice-free, that is, $U_{if}/U_{ic} = \sqrt[1/3]{2} = 1.27$. This reasoning anticipates a factor of 1.61 reduction in tidal kinetic energy during landfast ice periods (1.27^2). In Ryder Bay, during landfast ice cover, diurnal-band energy decreased by factors of between ~1.3 (Brearley et al., 2017) and ~2 (this study) of their ice-free value, values consistent with other data sets (Georgas, 2012; St-Laurent et al., 2008).

This line of reasoning was then upscaled (Section 3.3) to the whole Antarctic landfast under-ice boundary layer by combining the CATS2008 high resolution inverse tidal model (Padman et al., 2008), with the 1×1 km bi-weekly landfast ice cover maps (Fraser et al., 2020). Averaging over the calendar year of 2016 gives a lower bound on total power loss under all landfast ice around Antarctica of $T_{\text{LFI}} = 788$ MW. In other words, 0.788 GW is the mean rate-of-work of the barotropic tide on the underside of all landfast ice over the whole Antarctic during 2016. It is worth repeating that this is a lower-bound estimate. If one-third of landfast ice is dynamically formed, with an under-ice drag coefficient five times that of thermodynamically formed landfast ice (both reasonable), then this figure and our subsequent comparisons would rise by a factor of 7.5, giving $T_{\text{LFI}} \sim 6$ GW.

For a conservative estimate, the lower-bound of $T_{\text{LFI}} = 788$ MW may be compared with Antarctic shelf seas tidal energy dissipation rates computed from satellite altimetry, which vary from 10 to 47 GW (Egbert & Ray, 2001). Given that landfast ice occupies 1%–2% of the area of the Antarctic shelf seas, the estimate here of the rate of tidal work under landfast ice is reasonable, that is, 0.788 GW is 1.7% of an Antarctic tidal dissipation estimate of 47 GW. One caveat is that modeling of the seasonal under ice frictional effects on the barotropic tide in Hudson Bay (Georgas, 2012) showed significant reduction in barotropic tidal velocities during landfast ice covered periods, but also positional shifts of tidal co-phase lines. The method here does not account for feedback of under-ice friction on the spatial structure of the barotropic tide, though landfast ice spatial extent is small compared to barotropic tidal wavelength so any effect will likely be small.

In the global context, total dissipation of the barotropic tide is estimated at 3.7 TW (Munk & Wunsch, 1998), of which between 1.4 and 2.0 TW (Egbert & Ray, 2001) is estimated to be dissipated in the bottom boundary layers of shelf seas with about 47 GW attributed to the Antarctic shelf seas. Thus, by the (conservative) estimate made here, the underside of seasonal landfast Antarctic ice may presently contribute around 1.7% of Antarctic tidal dissipation and 0.06% of global tidal boundary layer dissipation. Insignificant contributions globally, but perhaps of significance to under-ice OSBL ecosystems when consideration is given to the concomitant loss of TKE energy input by the wind.

5.4. Wind Power Insulation

Other studies have reported a reduction in local wind-driven surface currents during periods of landfast ice cover (Ohshima et al., 2000; St-Laurent et al., 2008). Here we are interested more in changes to the direct input of TKE into the OSBL from the wind field, rather than momentum input. Our focus primarily is on the contrast in wind-induced TKE injection between ice-free and 100% landfast ice cover, however we also make estimates of wind work, E_0, in the region we have termed the MIOZ (mobile ice open ocean zone). The effect on air-sea stress of partial mobile pack ice cover therefore needs to be discussed and the size of the effect estimated. The effects of sea ice on wind stress are to modify the magnitude of momentum transfer, due to the differing drag coefficients of ice and water, and its direction due to an additional Ekman effect from the layer of ice (Fraser & Inall, 2018; Martin et al., 2014). We are more interested here in the first effect. In a modeling study of sea ice in the Arctic Ocean, Martin et al. (2014) find that the momentum transfer between air and ocean (that is the effective air/ocean stress), initially increases with sea ice concentration, c, peaking with a factor of ~ 2.1 (of the ice-free value) at around $c = 0.8$, before dropping off rapidly as sea ice cover becomes complete. The mean effect is a multiplicative factor on the ice-free wind stress value of ~ 1.6 (assuming a statistically normal distribution of sea ice concentration); a maximal effect would be an increase in ice-free wind stress on the ocean by a factor of 2.1 (assuming the entire MIOZ has $c = 0.8$, an unlikely situation). We do not include a multiplicative non-zero sea ice concentration factor for the MIOZ in what follows but note that it could increase the quoted values of ΣW_{MOIZ} and ΣW_{SLIZ} by a factor of ~ 1.6. As described in Section 3.4, ΣW_{MOIZ} represents an estimate of mean rate of working of the wind on the ocean over the MIOZ, disregarding the effects of mobile sea ice just discussed. ΣW_{SLIZ} (Section 3.4) is the rate at which TKE would have been injected into the SLIZ OSBL had there been no seasonal landfast ice cover. ΣW_{MOIZ} and ΣW_{SLIZ} are shown as annual averages for the full Antarctic region, and by sector (Table 1). ΣW_{MOIZ} and $T_{\text{LFI}}/\Sigma W_{\text{SLIZ}}$ are also shown as circum-Antarctic time series (Figure 8c).

The total rate of wind-generated TKE in the OSBL is greatly reduced by the presence of seasonal landfast ice to around 14% of the ice-free value ($\frac{T_{\text{LFI}}}{\Sigma W_{\text{SLIZ}}} = 0.14$; Table 1, Figure 8c). The effect is most pronounced in the WAP sector ($\frac{T_{\text{LFI}}}{\Sigma W_{\text{SLIZ}}} = 1.8\%$) and least pronounced in the Weddell Sea ($\frac{T_{\text{LFI}}}{\Sigma W_{\text{SLIZ}}} = 30\%$). These figures are of course hypothetical but are consistent with our observations of seasonal change in the WAP OSBL TKE, and serve to

illustrate some of the spatial and temporal variations in this profound regime shift between ice-free and landfast ice covered OSBL. An explanation for sectoral differences lies not in the average water depth beneath landfast ice formation, which varies little by sector (Table 1), but in the spatial distribution of barotropic tides (Figure 5); with large rms tide heights in the Weddell Sea (Padman et al., 2002), and contrasting weak tides on the WAP (Figure 5).

If one considers the region of the shelf seas around Antarctica stretching from the coastline to the maximal observed seasonal extent of landfast ice (LFImax) and compares the relative importance of wind versus tide in generating turbulence in the OSBL, then a quite different picture emerges (Table 1, Figure 8b). The processes now appear equally important, wind dominating in summer when ice cover is minimum, and tides dominant in winter when landfast ice extent is maximum. This is a quite remarkable and unexpected observation, showing the power of tidal friction in maintaining relatively high levels of OSBL turbulence year-round.

However, boundary-generated turbulence is very inefficient at eroding stratification not adjacent to the boundary, with an efficiency <0.1% (Simpson & Bowers, 1984). Therefore, even though the depth-integrated turbulence is enhanced under landfast ice, as we have seen it is concentrated in an under-ice boundary layer and not available to increase heat, buoyancy or nutrient fluxes from below. PWP mixing model simulations for year 2010 using SOSE, ERA5 and landfast ice maps allow estimations to be made of wind-induced heat flux from underlying waters into the OSBL, and a mixing rate-of-work on reducing the stratification (Section 3.5, Table 2, Figure 9). As expected, wind-work is seasonal, following the pattern of landfast ice cover. Heat fluxes are universally small. They are weakly negative in January and February, consistent with our observations of summertime wind-induced erosion of the sub-surface temperature minimum formed the previous winter. After erosion is complete, the remaining months the heat flux is weakly positive on spatial average. The values may be statistically indistinguishable from zero, but their sign is correct according to the vertical temperature gradient at the base of the OSBL. As a sense-check on these heat flux values, the time-rate-of-change of the OSBL depth integrated PE anomaly (Wm^{-2}) may be converted into a mixing work-rate by dividing by $\Gamma = 0.2$ (where $\Gamma = R_f/(1 - R_f)$ and $R_f = 0.17$ is the flux Richardson Number) and to an equivalent depth-averaged TKE dissipation rate by further dividing by an average OSBL thickness of 100 m and a conversion from m^3 to kg (Table 2, last two columns). TKE estimates so derived are similar to the rates observed in WAP wind-exposed OSBL (Figure 3).

Elevated turbulence in the under-ice OSBL is even less likely to impact vertical nutrient fluxes because landfast ice is established after the upper nitracline has been eroded by vertical mixing and surface nitrate values have reached, or at least are approaching, their winter maxima. The permanent nitracline between uCDW and the winter surface waters (50–200 m) is substantially deeper than the turbulent boundary layer, such that increased turbulence associated with landfast ice cover cannot access the higher nitrate concentrations in uCDW. However, increased turbulence in landfast ice boundary layers is likely to impact sympagic (ice-associated) biological communities, by altering exchanges of dissolved and particulate constituents between surface waters and the sea ice matrix, which often has nutrient concentrations significantly lower than the underlying waters (Cozzi, 2014; Fripiat et al., 2017). Enhanced nutrient supply associated with large tidal currents has been found to lead to high ice-algal biomass in the Canadian Arctic (Mortenson et al., 2017). If the high under ice turbulence identified here also increases nutrient supply to the sea ice environment, higher ice algal productivity and biological carbon uptake could result. The effects of underice turbulence would be more pronounced on sympagic rather than pelagic communities, because ice-algal growth starts earlier in the growing season when light returns to these latitudes and the ice-cover remains in place (Van Leeuwe et al., 2018). Increased boundary layer turbulence documented here might therefore increase biological productivity in the critical winter-to-spring transition, with positive impacts on carbon uptake and food supply to higher trophic levels.

6. Conclusion

In this article local measurements and careful analyses of those observations from a single WAP location in summer and in winter have been used to quantify the seasonal OSBL regime shift between ice and no ice. Using observationally constrained models and pan-Antarctic data sets of landfast ice we extend the insights gained at our sampling location in Ryder Bay to the whole Antarctic coastal zone. By the very nature of such up-scaling exercises, many details are lost. Much remains to be discovered about environment and ecosystems beneath landfast
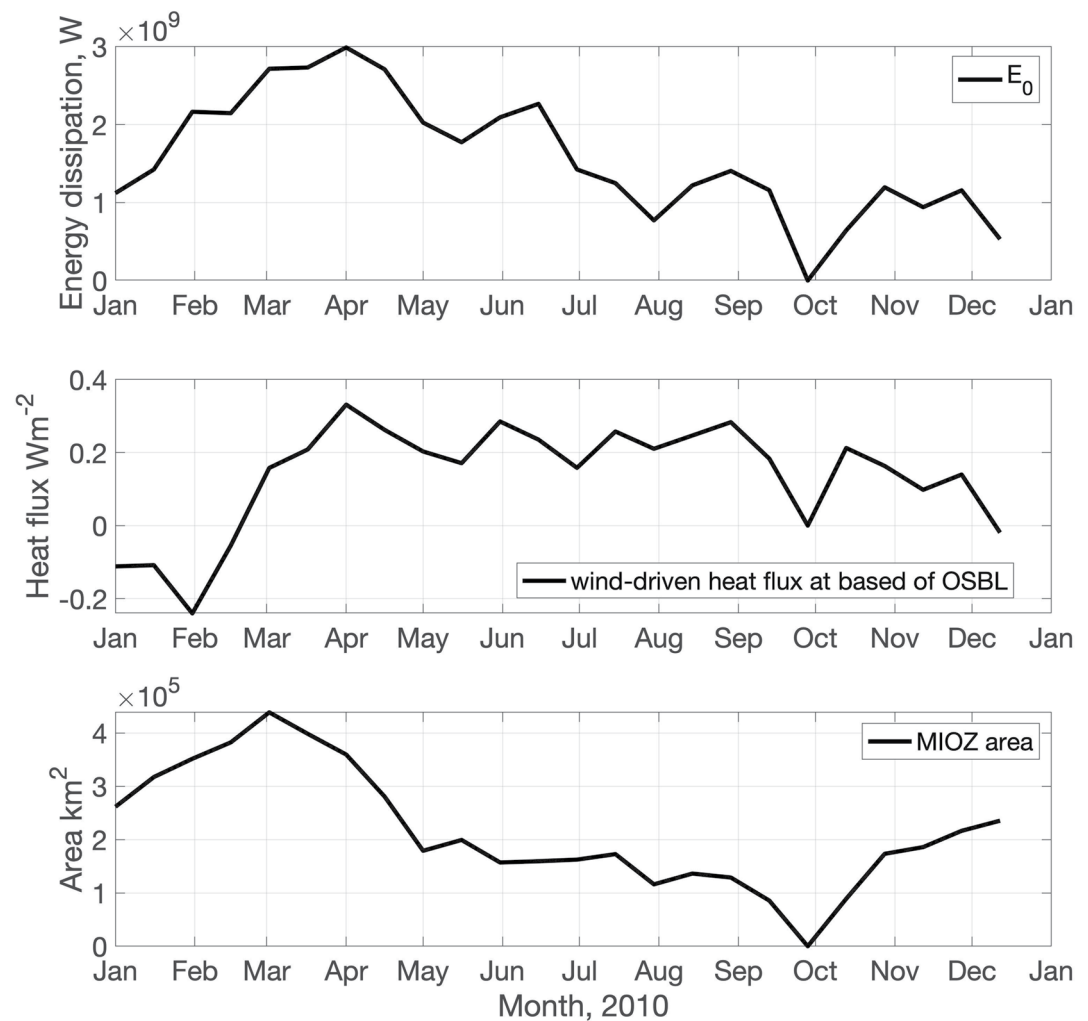
Figure 9. Upper panel: Wind power into the mobile ice/open ocean zone ocean surface boundary layer (OSBL) during 2010, derived from ERA5 reanalysis. Middle panel: Heat flux into the OSBL from below by wind-induced mixing derived using PWP mixing model. Lower panel: Circum-Antarctic landfast ice area extent during 2010 (Fraser et al., 2020).

ice; our aim is to offer some first reflections on the turbulent state of that environment–apparently as energetic due to under ice tidal stress, as by the wind action it replaces.

Data Availability Statement

Landfast ice data: https://doi.org/10.26179/5d267d1ceb60c. ERA5 data: https://cds.climate.copernicus.eu/cdsapp#!/home. CATS2008 is available for download through the U.S. Antarctic Program Data Center: Data doi: 10.15784/601235. Nutrients data: doi:10.5285/98cc0722-e337-029c-e053-6c86abc02029. Shear microstructure data: https://www.bodc.ac.uk/resources/inventories/edmed/report/6862/. RaTS CTD and ADCP data: https://www.bodc.ac.uk/resources/inventories/edmed/report/4278/. Southern Ocean State Estimate (SOSE): https://climatedataguide.ucar.edu/climate-data/southern-ocean-state-estimate-sose.

References

Alford, M. H. (2020). Revisiting near-inertial wind work: Slab models, relative stress, and mixed layer deepening. *Journal of Physical Oceanography*, *50*(11), 3141–3156. https://doi.org/10.1175/JPO-D-20-0105.1

Belcher, S. E., Grant, A. L. M., Hanley, K. E., Fox-Kemper, B., Van Roeke, L., Sullivan, P. P., et al. (2012). A global perspective on Langmuir turbulence in the ocean surface boundary layer. *Geophysical Research Letters*, *39*, L18605. https://doi.org/10.1029/2012GL052932

Brearley, J. A., Meredith, M. P., Naveira Garabato, A. C., Venables, H. J., & Inall, M. E. (2017). Controls on turbulent mixing on the West Antarctic Peninsula shelf. *Deep-Sea Research Part II Topical Studies in Oceanography*, *139*, 18–30. https://doi.org/10.1016/j.dsr2.2017.02.011

Clarke, A., Meredith, M. P., Wallace, M. I., Brandon, M. A., & Thomas, D. N. (2008). Seasonal and interannual variability in temperature, chlorophyll and macronutrients in northern Marguerite Bay, Antarctica. *Deep Sea Research Part II: Topical Studies in Oceanography*, *55*(18–19), 1988–2006. https://doi.org/10.1016/j.dsr2.2008.04.035

Cook, A. J., Holland, P. R., Meredith, M. P., Murray, T., Luckman, A., & Vaughan, D. G. (2016). Ocean forcing of glacier retreat in the western Antarctic Peninsula. *Science*, *353*(6296), 283–286. https://doi.org/10.1126/science.aae0017

Cozzi, S. (2014). Multiscale variability of ambient conditions, fast ice dynamics and biogeochemistry in the coastal zone of Victoria Land, Ross Sea. *Antarctic Science*, *26*(4), 427–444. https://doi.org/10.1017/S0954102013000813

Craig, P. D., & Banner, M. L. (1994). Modeling wave-enhanced turbulence in the ocean surface layer. *Journal of Physical Oceanography*, *24*(12), 2546–2559. https://doi.org/10.1175/1520-0485(1994)024<2546:mwetit>2.0.co;2

Dewey, R. K., & Crawford, W. R. (1988). Bottom stress estimates from vertical dissipation rate profiles on the continental-shelf. *Journal of Physical Oceanography*, *18*(8), 1167–1177. https://doi.org/10.1175/1520-0485(1988)018<1167:bsefvd>2.0.co;2

Egbert, G. D., & Ray, R. D. (2000). Significant dissipation of tidal energy in the deep ocean inferred from satellite altimeter data. *Nature*, *405*(6788), 775–778. https://doi.org/10.1038/35015531

Egbert, G. D., & Ray, R. D. (2001). Estimates of M2 tidal energy dissipation from TOPEX/Poseidon altimeter data. *Journal of Geophysical Research*, *106*(C10), 22475–22502. https://doi.org/10.1029/2000jc000699

Evans, D. G., Lucas, N. S., Hemsley, V., Frajka-Williams, E., Garabato, A. C. N., Martin, A., et al. (2018). Annual cycle of turbulent dissipation estimated from seagliders. *Geophysical Research Letters*, *45*(19), 10–560. https://doi.org/10.1029/2018gl079966

Fairall, C. W., Bradley, E. F., Hare, J. E., Grachev, A. A., & Edson, J. B. (2003). Bulk parameterization of air-sea fluxes: Updates and verification for the COARE algorithm. *Journal of Climate*, *16*(4), 571–591. https://doi.org/10.1175/1520-0442(2003)016<0571:BPOASF>2.0.CO;2

Fer, I., & Sundfjord, A. (2007). Observations of upper ocean boundary layer dynamics in the marginal ice zone. *Journal of Geophysical Research*, *112*(C4). https://doi.org/10.1029/2005JC003428

Fraser, A. D., Massom, R. A., Handcock, M. S., Reid, P., Ohshima, K. I., Raphael, M. N., et al. (2021). Eighteen-year record of circum-Antarctic landfast-sea-ice distribution allows detailed baseline characterisation and reveals trends and variability, *The Cryosphere*, *15*, 5061–5077, https://doi.org/10.5194/tc-15-5061-2021

Fraser, A. D., Massom, R. A., Michael, K. J., Galton-Fenzi, B. K., & Lieser, J. L. (2012). East Antarctic landfast sea ice distribution and variability, 2000–2008. *Journal of Climate*, *25*(4), 1137–1156. https://doi.org/10.1175/JCLI-D-10-05032.1

Fraser, A. D., Massom, R. A., Ohshima, K. I., Willmes, S., Kappes, P. J., Cartwright, J., & Porter-Smith, R. (2020). High-resolution mapping of circum-Antarctic landfast sea ice distribution, 2000–2018. *Earth System Science Data*, *12*(4), 2987–2999. https://doi.org/10.5194/essd-12-2987-2020

Fraser, N. J., & Inall, M. E. (2018). Influence of barrier wind forcing on heat delivery toward the Greenland ice sheet. *Journal of Geophysical Research: Oceans*, *123*, 2513–2538. https://doi.org/10.1002/2017JC013464

Fripiat, F., Meiners, K. M., Vancoppenolle, M., Papadimitriou, S., Thomas, D. N., Ackley, S. F., et al. (2017). Macro-nutrient concentrations in Antarctic pack ice: Overall patterns and overlooked processes. *Elementa: Science of the Anthropocene*, *5*. https://doi.org/10.1525/elementa.217

Gargett, A. E. (1985). Evolution of scalar spectra with the decay of turbulence in a stratified fluid. *Journal of Fluid Mechanics*, *159*, 379–407. https://doi.org/10.1017/s0022112085003263

Georgas, N. (2012). Large seasonal modulation of tides due to ice cover friction in a midlatitude estuary. *Journal of Physical Oceanography*, *42*, 352–369. https://doi.org/10.1175/JPO-D-11-063.1

Giles, A. B., Massom, R. A., & Lytle, V. I. (2008). Fast-ice distribution in East Antarctica during 1997 and 1999 determined using RADARSAT data. *Journal of Geophysical Research*, *113*(C2), C02S14. https://doi.org/10.1029/2007JC004139

Henley, S. F., Cavan, E. L., Fawcett, S. E., Kerr, R., Monteiro, T., Sherrell, R. M., et al. (2020). Changing biogeochemistry of the southern ocean and its ecosystem implications. *Frontiers in Marine Science*, *7*. https://doi.org/10.3389/fmars.2020.00581

Henley, S. F., Jones, E. M., Venables, H. J., Meredith, M. P., Firing, Y. L., Dittrich, R., et al. (2018). Macronutrient and carbon supply, uptake and cycling across the Antarctic Peninsula shelf during summer. *Philosophical Transactions of the Royal Society A: Mathematical, Physical and Engineering Sciences*, *376*(2122), 20170168. https://doi.org/10.1098/rsta.2017.0168

Henley, S. F., Schofield, O. M., Hendry, K. R., Schloss, I. R., Steinberg, D. K., Moffat, C., et al. (2019). Variability and change in the West Antarctic Peninsula marine system: Research priorities and opportunities. *Progress in Oceanography*, *173*, 208–237. https://doi.org/10.1016/j.pocean.2019.03.003

Henley, S. F., Tuerena, R. E., Annett, A. L., Fallick, A. E., Meredith, M. P., Venables, H. J., et al. (2017). Macronutrient supply, uptake and recycling in the coastal ocean of the west Antarctic Peninsula. *Deep Sea Research Part II: Topical Studies in Oceanography*, *139*, 58–76. https://doi.org/10.1016/j.dsr2.2016.10.003

Hersbach, H., Bell, B., Berrisford, P., Hirahara, S., Horányi, A., Muñoz-Sabater, J., et al. (2020). The ERA5 global reanalysis. *Quarterly Journal of the Royal Meteorological Society*, *146*(730), 1999–2049. https://doi.org/10.1002/qj.3803

Howard, S. L., Hyatt, J., & Padman, L. (2004). Mixing in the pycnocline over the Western Antarctic Peninsula shelf during Southern Ocean GLOBEC. *Deep Sea Research Part II: Topical Studies in Oceanography*, *51*(17–19), 1965–1979. https://doi.org/10.1016/j.dsr2.2004.08.002

Lozovatsky, I. (2005). Observations and scaling of the upper mixed layer in the North Atlantic. *Journal of Geophysical Research*, *110*(C5), C05013. https://doi.org/10.1029/2004JC002708

Lu, P., Li, Z., Cheng, B., & Leppäranta, M. (2011). A parameterization of the ice-ocean drag coefficient. *Journal of Geophysical Research*, *116*(C7), C07019. https://doi.org/10.1029/2010JC006878

Lucas, N. S., Grant, A. L. M., Rippeth, T. P., Polton, J. A., Palmer, M. R., Brannigan, L., & Belcher, S. E. (2019). Evolution of oceanic near-surface stratification in response to an autumn storm. *Journal of Physical Oceanography*, *49*(11), 2961–2978. https://doi.org/10.1175/JPO-D-19-0007.1

Martin, T., Steele, M., & Zhang, J. (2014). Seasonality and long-term trend of Arctic Ocean surface stress in a model. *Journal of Geophysical Research: Oceans*, *119*(3), 1723–1738. https://doi.org/10.1002/2013JC009425

Mazloff, M. R., Heimbach, P., & Wunsch, C. (2010). An eddy-permitting Southern Ocean state estimate. *Journal of Physical Oceanography*, *40*(5), 880–899. https://doi.org/10.1175/2009JPO4236.1

McPhee, M. G. (1999). Parameterization of mixing in the ocean boundary layer. *Journal of Marine Systems*, (*21*, 55–65). https://doi.org/10.1016/S0924-7963(99)00005-6

McPhee, M. G. (2008). *Air-ice-ocean interaction*. Springer.

Moffat, C., & Meredith, M. (2018). Shelf-ocean exchange and hydrography west of the Antarctic Peninsula: A review. *Philosophical Transactions of the Royal Society A: Mathematical, Physical and Engineering Sciences*, *376*, 20170164. https://doi.org/10.1098/rsta.2017.0164

Moffat, C., Owens, B., & Beardsley, R. C. (2009). On the characteristics of circumpolar deep water intrusions to the west Antarctic Peninsula continental shelf. *Journal of Geophysical Research*, *114*(C5), C05017. https://doi.org/10.1029/2008JC004955

Mortenson, E., Hayashida, H., Steiner, N., Monahan, A., Blais, M., Gale, M. A., et al. (2017). A model-based analysis of physical and biological controls on ice algal and pelagic primary production in Resolute Passage. *Elementa: Science of the Anthropocene*, *5*, 39. https://doi.org/10.1525/elementa.229

Munk, W., & Wunsch, C. (1998). Abyssal recipes II: Energetics of tidal and wind mixing. *Deep-Sea Research*, *45*, 1977–2010. https://doi.org/10.1016/s0967-0637(98)00070-3

Oakey, N. S., & Elliott, J. A. (1982). Dissipation within the surface mixed layer. *Journal of Physical Oceanography*, *12*(2), 171–185. https://doi.org/10.1175/1520-0485(1982)012<0171:DWTSML>2.0.CO;2

Ohshima, K. I., Kawamura, T., Takizawa, T., Ushio, S., & Miyakawa, T. (2000). Current variability under landfast sea ice in Lützow-Holm Bay, Antarctica. *Journal of Geophysical Research*, *105*(C7), 17121–17132. https://doi.org/10.1029/2000JC900080

Osborn, T. R. (1980). Estimates of the local rate of vertical diffusion from dissipation measurements. *Journal of Physical Oceanography*, *10*, 83–89. https://doi.org/10.1175/1520-0485(1980)010<0083:eotlro>2.0.co;2

Padman, L., Erofeeva, S. Y., & Fricker, H. A. (2008). Improving Antarctic tide models by assimilation of ICESat laser altimetry over ice shelves. *Geophysical Research Letters*, *35*(22), L22504. https://doi.org/10.1029/2008GL035592

Padman, L., Fricker, H. A., Coleman, R., Howard, S., & Erofeeva, L. (2002). A new tide model for the Antarctic ice shelves and seas. *Annals of Glaciology*, *34*, 247–254. https://doi.org/10.3189/172756402781817752

Prandke, H., & Stipps, A. (1998). A microstructure profiler to study mixing and turbulent transport processes. In *IEEE oceans 1998*, (Vol. 1, pp. 179–183).

Prézelin, B. B., Hofmann, E. E., Mengelt, C., & Klinck, J. M. (2000). The linkage between upper circumpolar deep water (UCDW) and phytoplankton assemblages on the west Antarctic Peninsula continental shelf. *Journal of Marine Research*, *58*(2), 165–202. https://doi.org/10.1357/002224000321511133

Price, J. F., Weller, R. A., & Pinkel, R. (1986). Diurnal cycling: Observations and models of the upper ocean response to diurnal heating, cooling, and wind mixing. *Journal of Geophysical Research*, *91*(C7), 8411–8427. https://doi.org/10.1029/JC091iC07p08411

Randelhoff, A., Fer, I., & Sundfjord, A. (2017). Turbulent upper-ocean mixing affected by meltwater layers during arctic summer. *Journal of Physical Oceanography*, *47*(4), 835–853. https://doi.org/10.1175/JPO-D-16-0200.1

Rippeth, T. P., & Inall, M. E. (2002). Observations of the internal tide and associated mixing across the Malin Shelf. *Journal of Geophysical Research*, *107*(C4). https://doi.org/10.1029/2000jc000761

Segal, R. A., Scharien, R. K., Cafarella, S., & Tedstone, A. (2020). Characterizing winter landfast sea-ice surface roughness in the Canadian Arctic Archipelago using Sentinel-1 synthetic aperture radar and the Multi-angle Imaging SpectroRadiometer. *Annals of Glaciology*, *61*(83), 284–298. https://doi.org/10.1017/aog.2020.48

Serebrennikova, Y. M., & Fanning, K. A. (2004). Nutrients in the Southern Ocean GLOBEC region: Variations, water circulation, and cycling. *Deep Sea Research Part II: Topical Studies in Oceanography*, *51*(17–19), 1981–2002. https://doi.org/10.1016/j.dsr2.2004.07.023

Sharples, J., Tweddle, J. F., Green, J. A. M., Palmer, M. R., Kim, Y. N., Hickman, A. E., et al. (2007). Spring-neap modulation of internal tide mixing and vertical nitrate fluxes at a shelf edge in summer. *Limnology and Oceanography*, *52*(5), 1735–1747. https://doi.org/10.4319/lo.2007.52.5.1735

Shih, L. H., Koseff, J. R., Ivey, G. N., & Ferziger, J. H. (2005). Parameterisation of turbulent fluxes and scales using homogeneous sheard stratified turbulence simulations. *Journal of Fluid Mechanics*, *525*, 193–214. https://doi.org/10.1017/S0022112004002587

Simpson, J. H., & Bowers, D. G. (1984). The role of tidal stirring in controlling the seasonal heat cycle in shelf seas. *Annales Geophysicae*, *2*(4), 411–416.

Simpson, J. H., Crawford, W. R., Rippeth, T. P., Campbell, A. R., & Cheok, J. V. S. (1996). The vertical structure of turbulent dissipation in shelf seas. *Journal of Physical Oceanography*, *26*(8), 1579–1590. https://doi.org/10.1175/1520-0485(1996)026<1579:tvsotd>2.0.co;2

St-Laurent, P., Saucier, F. J., & Dumais, J. F. (2008). On the modification of tides in a seasonally ice-covered sea. *Journal of Geophysical Research*, *113*(C11). https://doi.org/10.1029/2007JC004614

Van Leeuwe, M., Tedesco, L., Arrigo, K. R., Assmy, P., Campbell, K., Meiners, K. M., et al. (2018). Microalgal community structure and primary production in Arctic and Antarctic Sea ice: A synthesis. *Elementa: Science of the Anthropocene*, *6*(1), 4. https://doi.org/10.1525/elementa.267

Venables, H. J., Clarke, A., & Meredith, M. P. (2013). Wintertime controls on summer stratification and productivity at the western Antarctic Peninsula. *Limnology and Oceanography*, *58*, 1035–1047. https://doi.org/10.4319/lo.2013.58.3.1035

Venables, H. J., & Meredith, M. P. (2014). Feedbacks between ice cover, ocean stratification, and heat content in Ryder Bay, Western Antarctic Peninsula. *Journal of Geophysical Research: Oceans*, *119*(8), 5323–5336. https://doi.org/10.1002/2013JC009669

Venables, H. J., Meredith, M. P., & Brearley, J. A. (2017). Modification of deep waters in Marguerite Bay, western Antarctic Peninsula, caused by topographic overflows. *Deep Sea Research Part II: Topical Studies in Oceanography*, *139*, 9–17. https://doi.org/10.1016/j.dsr2.2016.09.005

Wallace, M. I., Meredith, M. P., Brandon, M., Sherwin, T. J., Dale, A. C., & Clarke, A. (2008). On the characteristics of internal tides and coastal upwelling behaviour in Marguerite Bay, West Antarctic Peninsula. *Deep Sea Research II*, *55*, 2023–2040. https://doi.org/10.1016/j.dsr2.2008.04.033

Weston, K., Jickells, T. D., Carson, D. S., Clarke, A., Meredith, M. P., Brandon, M. A., et al. (2013). Primary production export flux in Marguerite Bay (Antarctic Peninsula): Linking upper water-column production to sediment trap flux. *Deep Sea Research Part I: Oceanographic Research Papers*, *75*, 52–66. https://doi.org/10.1016/j.dsr.2013.02.001

Wu, J. (1983). Sea-surface drift currents induced by wind and waves. *Journal of Physical Oceanography*, *13*(8), 1441–1451. https://doi.org/10.1175/1520-0485(1983)013<1441:SSDCIB>2.0.CO;2